ADVANCED FUNCTIONAL MATERIALS
www.afm-journal.de

Understanding the Origin of Li_2MnO_3 Activation in Li-Rich Cathode Materials for Lithium-Ion Batteries

*Delai Ye, Guang Zeng, Kazuhiro Nogita, Kiyoshi Ozawa, Marlies Hankel, Debra J. Searles, and Lianzhou Wang**

Li-rich layered cathode materials have been considered as a family of promising high-energy density cathode materials for next generation lithium-ion batteries (LIBs). However, although activation of the Li_2MnO_3 phase is known to play an essential role in providing superior capacity, the mechanism of activation of the Li_2MnO_3 phase in Li-rich cathode materials is still not fully understood. In this work, an interesting Li-rich cathode material $Li_{1.87}Mn_{0.94}Ni_{0.19}O_3$ is reported where the Li_2MnO_3 phase activation process can be effectively controlled due to the relatively low level of Ni doping. Such a unique feature offers the possibility of investigating the detailed activation mechanism by examining the intermediate states and phases of the Li_2MnO_3 during the controlled activation process. Combining powerful synchrotron in situ X-ray diffraction analysis and observations using advanced scanning transmission electron microscopy equipped with a high angle annular dark field detector, it has been revealed that the subreaction of O_2 generation may feature a much faster kinetics than the transition metal diffusion during the Li_2MnO_3 activation process, indicating that the latter plays a crucial role in determining the Li_2MnO_3 activation rate and leading to the unusual stepwise capacity increase over charging cycles.

1. Introduction

In the past decade, electric vehicles (EVs) have made significant progress toward commercialization. However, the high price of EVs is still a large barrier to replace the traditional cars, mainly due to the lack of cheap and high-energy batteries. Lithium ion batteries (LIBs) are the most popular power sources for portable electronics and have been generally considered as the most potential power source to EVs.[1–3] Currently, numerous anode materials with high specific capacities (more than 1000 mAh g^{-1}) and high power density have been developed for LIBs;[4–6] however, the specific capacities of the benchmark cathode materials, such as $LiCoO_2$, $LiFePO_4$, and $LiMn_2O_4$, are still limited to <150 mAh g^{-1}, being the bottleneck of the LIB system.[7]

Li-rich layered cathode materials have attracted much recent attention due to their extraordinary high specific capacity of more than 250 mAh g^{-1} at room temperature. Generally, they are described as $xLi_2MnO_3\cdot(1-x)LiMO_2$ (M = Mn, Ni, Co or their mixture), in which the Li_2MnO_3 can be activated by high voltage charging to provide the extra capacity.[8] To meet the demand of practical applications, there are still significant challenges associated with the Li-rich cathode materials including the poor long-term cycling stability, low power density, and voltage decline, and some advanced techniques such as surface coating and modification have been well developed to overcome these problems.[9,10] But more importantly, the fundamental understanding of the electrochemical reactions and the corresponding crystal structure evolutions of the Li-rich materials have still not been fully revealed due to the complexity of their compositions and structures.[11–14]

Li-rich materials within the Li–Ni–Mn–O system are favorable because of the absence of expensive and toxic Co. Among them, the $Li_{1.2}Mn_{0.6}Ni_{0.2}O_2$ material has been well studied as a representative composition.[15,16] A long and flat plateau is featured from around 4.5 to 4.8 V during the 1st charge, and the activation of the Li_2MnO_3 phase has been demonstrated to be the intrinsic reason for such a long plateau which involves a few subreactions including Li^+ extraction from both the Li and the transition metal (TM) layers, oxygen release from the crystal lattice, and the TM ion diffusion into the Li

Dr. D. Ye, Prof. L. Wang
Nanomaterials Centre
School of Chemical Engineering and Australian Institute of Bioengineering and Nanotechnology
The University of Queensland
Brisbane QLD 4072, Australia
E-mail: l.wang@uq.edu.au
Dr. G. Zeng, Prof. K. Nogita
Nihon Superior Centre for the Manufacture of Electronic Materials (NS CMEM)
School of Mechanical and Mining Engineering
The University of Queensland
Brisbane QLD 4072, Australia
Dr. K. Ozawa
National Institute for Materials Science
Tsukuba, Ibaraki 305-0047, Japan
Dr. M. Hankel, Prof. D. J. Searles
AIBN Centre for Theoretical and Computational Molecular Science
The University of Queensland
Brisbane QLD 4072, Australia
Prof. D. J. Searles
School of Chemistry and Molecular Biosciences
The University of Queensland
Brisbane QLD 4072, Australia

DOI: 10.1002/adfm.201503276

layers.[16–18] However, as the Li_2MnO_3 phase is often completely activated in the 1st cycle, it is difficult to investigate these subreactions separately, therefore, in most cases, they are basically considered to occur simultaneously as a whole reaction.[19] In our recent work, it was found that the rate of Li_2MnO_3 phase activation could be adjusted by controlling the doping level of Ni or Co.[20,21] The incomplete Li_2MnO_3 activation process in the initial cycles can provide an excellent opportunity to study the intermediate state, phase and subreactions of the Li-rich cathode materials.

Based on a Ni-poor Li-rich cathode material providing controlled Li_2MnO_3 activation rate, we report a detailed study on the reaction kinetics involved in the Li_2MnO_3 activation by a combined electrochemical analysis and structural characterization. A prominent oxygen-generation plateau was observed in the 1st charge above 4.6 V, accompanied by Li extraction from only the Li layers as indicated by the continuous expansion of the *c*-parameter. Meanwhile, no change of the Li-TM ordering in the TM layer can be detected in the synchrotron in situ X-ray diffraction (XRD) pattern. From the sectional charge/discharge capacity investigation and high angle annular dark-field scanning transmission electron microscopy (HAADF-STEM) observations, it was also found that although the oxygen release plateau disappeared within the initial 5 cycles, the Li_2MnO_3 activation process continued for many more cycles with gradual capacity increase, crystal structure evolution, consequent voltage decline, and growth of TMs in the Li layers, strongly indicating that the two subreactions of oxygen release and TM ion rearrangement do not occur concurrently, and the latter is the key kinetic step in the Li_2MnO_3 activation and results in the unusual phenomenon of gradual capacity increase. These findings can help to better understand the electrochemical activation mechanism and kinetics of the Li_2MnO_3 phase and the corresponding structure transformation in Li-rich cathode materials. More importantly, they also provide clues to guide the exploration of cost-effective and high-energy cathode materials for high-performance LIBs.

2. Results and Discussion

The composition of the material was determined to be $Li_{1.25}Mn_{0.625}Ni_{0.125}O_2$ by ICP-AES analysis. As shown in **Figure 1**a, all the main diffraction peaks are sharp, clear, and well fitted with the typical layered *R*-3*m* space group (JCPDS No. 84–1634) except for a few minor peaks located between 20° and 25° (marked in red in Figure 1a), which are due to a localized $LiTM_6$ superlattice in the Li_2MnO_3-like monoclinic structure.[8,22,23] It has been well accepted that Li_2MnO_3 is a more common notation of $Li[Li_{1/3}Mn_{2/3}]O_2$, in which 1/3 of the Mn in the TM layers of typical layered $LiMnO_2$ structure are replaced by Li.[8] Here in our $Li_{1.25}Mn_{0.625}Ni_{0.125}O_2$ material, considering its close crystal structure with Li_2MnO_3 as indicated by XRD study, it will be notated as $Li_{1.87}Mn_{0.94}Ni_{0.19}O_3$ in the following content. A high (003)/(104) peak intensity ratio (>1.2) can be clearly observed with well split (006)/(012) and (018)/(110) peaks pairs, suggesting a low degree of TM ions in the Li layers.[24] All these observations demonstrate a highly crystalline material with a typical layered monoclinic structure. To identify the valence state of Mn and Ni in the pristine $Li_{1.87}Mn_{0.94}Ni_{0.19}O_3$ composite, X-ray photoelectron spectrometry (XPS) was performed and the spectra of Mn- and Ni-2p is shown in Figure 1b,c. The Mn $2p_{3/2}$ binding energy is around 642.2 eV, which is consistent with that of Mn^{4+}.[25,26] Generally, the Ni $2p_{3/2}$ energy in XPS is around 854 eV for Ni^{2+} and 856 eV for Ni^{3+}. The Ni $2p_{3/2}$ energy here is located at 854.9 eV, indicating

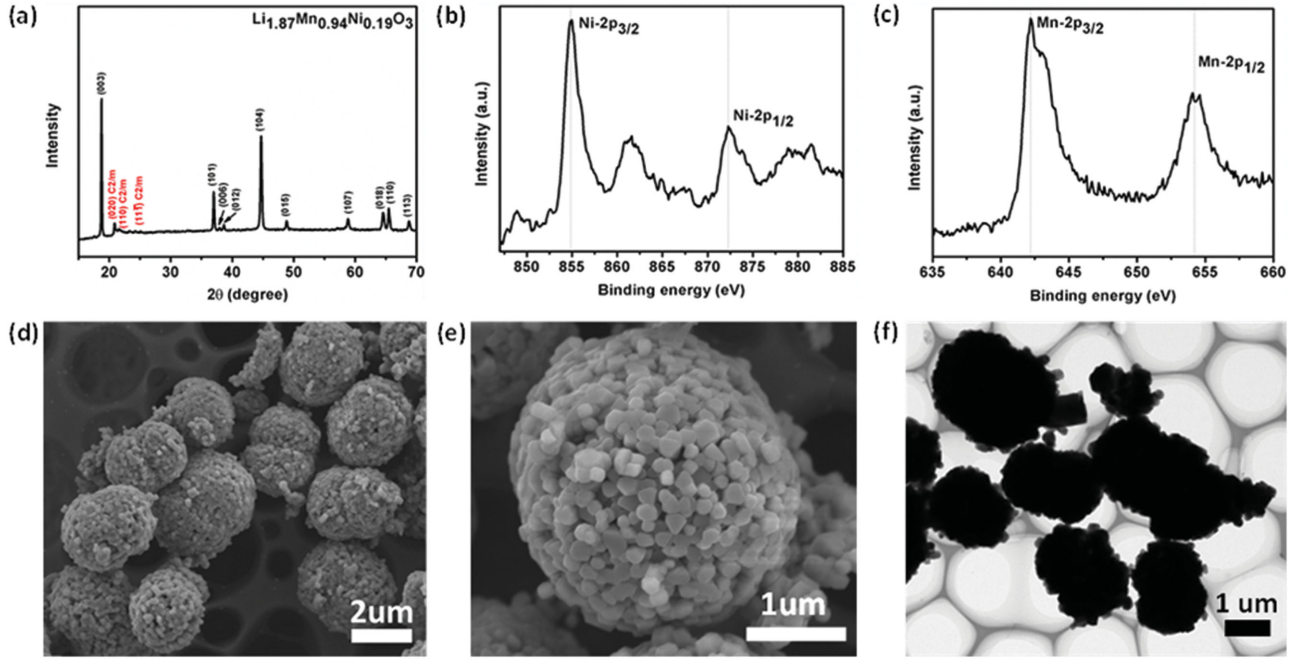

Figure 1. a) Powder X-ray diffraction pattern; b,c) XPS spectra of Mn_{2p} and Ni_{2p}; d,e) FE-SEM images; f) TEM image of the pristine $Li_{1.87}Mn_{0.94}Ni_{0.19}O_3$ composite.

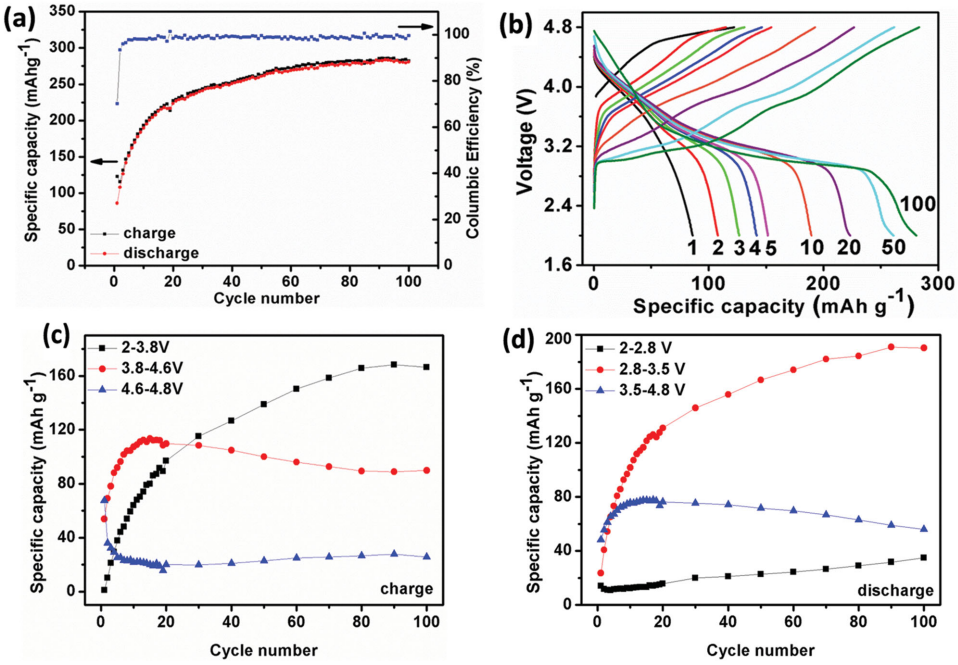

Figure 2. a) Charge and discharge capacities and the corresponding Columbic efficiency (blue points) of the $Li_{1.87}Mn_{0.94}Ni_{0.19}O_3$ material in the first 100 cycles at 30 mA g^{-1} between 2 and 4.8 V. b) Detailed charge/discharge curves of this material in some typical cycles. c) Net charge capacities in the voltage ranges of 2–3.8, 3.8–4.6, and 4.6–4.8 V; and d) net discharge capacities in the voltage ranges of 4.8–3.5, 3.5–2.8, and 2.8–2 V in the first 100 cycles.

the coexistence of both Ni^{2+} and Ni^{3+}.[27–29] Considering the composition of $Li_{1.87}Mn_{0.94}Ni_{0.19}O_3$ from ICP-AES analysis, a larger portion of Ni^{2+} and a trace amount of Mn^{3+} is expected to maintain the charge neutrality of the material. The morphology and microstructure of the pristine $Li_{1.87}Mn_{0.94}Ni_{0.19}O_3$ composite were observed by field-emission scanning electron microscope (FE-SEM) as shown in Figure 1d,e. Spherical microparticles can be seen with a diameter of around 2 to 3 µm. With a higher magnification, it is found they are in fact porous nanocrystals formed from subunits of around 100 nm. Such a hierarchical microstructure is also confirmed in the TEM image (Figure 1f) where 2–3 µm particles present with rough surfaces. This is advantageous for cathode materials because they can accommodate the lattice strain of the crystal structures during long term cycling and concurrently provide sufficient surface area for electrode-electrolyte contact.[30,31]

The $Li_{1.87}Mn_{0.94}Ni_{0.19}O_3$ material was electrochemically tested in a coin cell at room temperature under a current density of 30 mA g^{-1} (0.1C) between 2 and 4.8 V (**Figure 2**a). Interestingly, both the specific charge and discharge capacities of this material continuously increased from ≫100 mAh g^{-1} in the 1st cycle to nearly 220 mAh g^{-1} in the 20th cycle, and then exhibited a smooth continual increase until the 100th cycle where the capacity is about 280 mAh g^{-1}. This phenomenon of a prominent capacity increase over cycles has been attributed to the relatively small amounts of Ni or Co, which are not sufficient to completely activate the Li_2MnO_3 in the first cycle and results in the gradual capacity increase over quite a few cycles and the associated phase transformation from the parent layered structure to a new spinel phase.[20,32] It should be noted that the Columbic efficiency of this material did not have a gradual increase. Like most of the Li-rich materials, it was relatively low in the 1st cycle and then jumped up drastically to more than 90% in the 2nd cycle and rapidly became stable at almost 100% after the 5th cycle. Such a low 1st-cycle efficiency has been reported to originate from the partially irreversible reactions involving the simultaneous release of oxygen and extraction of Li during the high-voltage charging process in the 1st cycle.[8,16]

Further information of typical charge/discharge curves are presented in Figure 2b. In the 1st charge curve, two plateaus can be clearly identified. In the first one from 2–4.6 V, a specific charge capacity of 55.1 mAh g^{-1} was achieved. This is mainly due to the oxidation of Ni^{2+} to Ni^{3+} and Ni^{4+}, and possibly also the oxidation of a minor residual of Mn^{3+} to Mn^{4+}. The second high-voltage charging plateau from 4.6–4.8 V is characteristic of the lattice oxygen release in Li-rich cathode materials as has been well demonstrated in the literature.[16,17] Here in our $Li_{1.87}Mn_{0.94}Ni_{0.19}O_3$ material, this plateau can be clearly seen in the 1st charge curve as a long and flat tail, delivering a specific charge capacity of 67.2 mAh g^{-1}. In fact, our materials $Li_{1.87}Mn_{0.94}Ni_{0.19}O_3$ can also be formulated as $2/3Li_2MnO_3$–$1/3Li[Mn_{1/2}Ni_{1/2}]O_2$, where the weight percentage of Li_2MnO_3 is about 71%. Suppose all the specific capacity above 4.6 V in the first charge is from Li_2MnO_3 activation, it can be roughly estimated that 20% of the Li_2MnO_3 was activated in the first cycle (theoretical specific capacity of Li_2MnO_3 activation to generate Li_2O and MnO_2 is 458.6 mAh g^{-1}). After the first cycle, this long and flat plateau above 4.6 V gets shorter quickly and disappears after 5 cycles.

In the following cycles, the charge curves gradually evolve into two slopes with one from 2.9 to 3.6 V and the other from

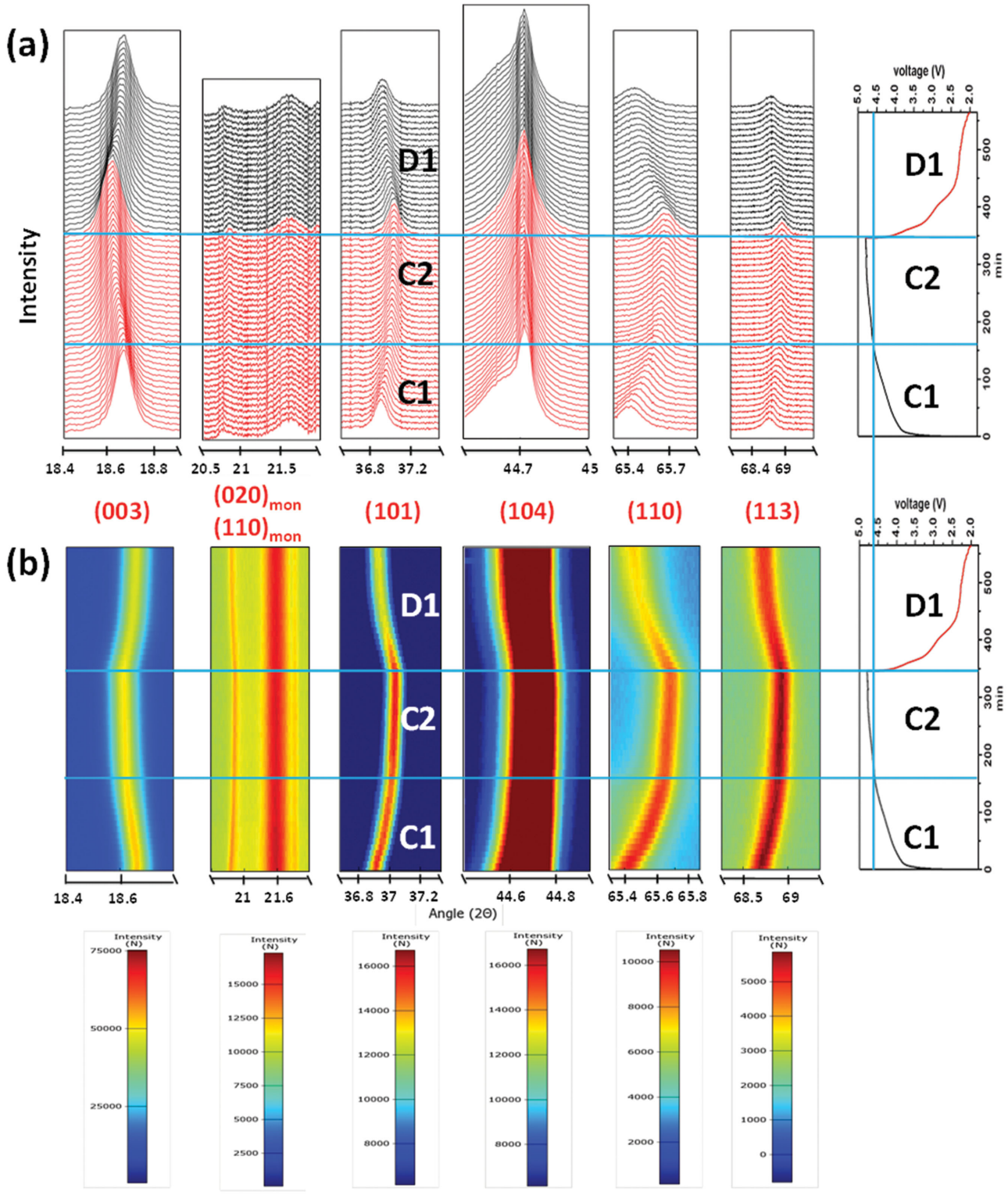

Figure 3. Selected area in situ XRD patterns and corresponding 1st cycle charge/discharge profile versus time of the $Li_{1.87}Mn_{0.94}Ni_{0.19}O_3$ composite. a) The stacked in situ XRD patterns and b) the color-coded, time-resolved, intensity distribution plots with reference color bar underneath.

3.6 to 4.8 V. The former slope regularly evolved from nothing in the first charge to a long and flat one at the end of the 100th cycle in which a charge capacity of about 141.4 mAh g^{-1} was achieved. Considering the total charge capacity increase of 159.1 mAh g^{-1} in the 100th cycle, it is clear that the charge capacity mainly increased in this slope region. In contrast, the latter slope had just a minor increase in length, but experienced a significantly change in shape. On the other side, the two plateaus observed during the first charge were integrated into a smooth one after just 5 cycles and this was then maintained afterward, indicating cease of the high-voltage oxygen release reaction within the initial 5 cycles. Note that it would be complicated to quantitatively estimate the total amount of oxygen generation in the initial 5 cycles, because a significant part of the charge capacities above 4.6 V may not be contributed by the oxygen generation from the 2nd cycle to the 5th cycle. Similarly, the discharge curves continually elongated over cycles. The growth mainly occurs in the 3 V region, which finally forms a dominating 3 V plateau. Together with the gradually developed 3.2 V charge slope, this implies gradual phase transformation to a new spinel phase during cycling.[33,34] In addition, a decrease in the discharge voltage between 3 and 3.8 V during cycling may be noted. Such a voltage drop has been proposed to be related to a hysteresis phenomenon that also signifies an irreversible phase transformation with TM ion diffusion in the Li-rich cathode materials.[35,36]

To have a more straightforward comparison of the capacity evolution, both the charge and discharge curves are split into three voltage regions corresponding to different redox reactions and the varying tendency of the specific capacity in each region during cycling has been plotted in Figure 2c,d. For the charge process, although the whole capacity increased with the number of cycles, the capacity in the region of 4.6–4.8 V actually decreased significantly in the initial 5 cycles and then kept almost stable for the rest of cycles, further implying that the high-voltage oxygen-release reaction in our material is highly irreversible and finished in the initial 5 cycles. The charge capacities at 2–3.8 V and discharge capacities at 3.5–2.8 V are characteristic of a new spinel phase induced by TM diffusion to the Li layers. And both of them present very similar trend of continuous increase in the first 100 cycles. Meanwhile, the charge capacities at 3.8–4.6 V and discharge capacities at 4.8–3.5 V mainly involve the Li extraction from and Li insertion into the Li layers of the original layered phase. And they gradually decreased over cycles. All the behaviors of charge and discharge capacities in these typical regions indicate a continuous TM diffusion process and consequent phase evolution from layered one to the spinel-like phase over the whole 100 cycles. Based on the electrochemical analysis, it appears that the TM diffusion process may feature a much slower kinetics than the oxygen release reaction.

In situ XRD is a powerful technique to monitor the real-time structural transformation and lattice change of inorganic electrode materials during electrochemical reactions. To further understand the crystal structure changes of our $Li_{1.87}Mn_{0.94}Ni_{0.19}O_3$ material during the 1st cycle between 2 and 4.8 V, in situ XRD measurement was conducted (**Figure 3**). For the convenience of comparison, the 1st cycle is divided into three sections by blue lines in both Figure 3 and

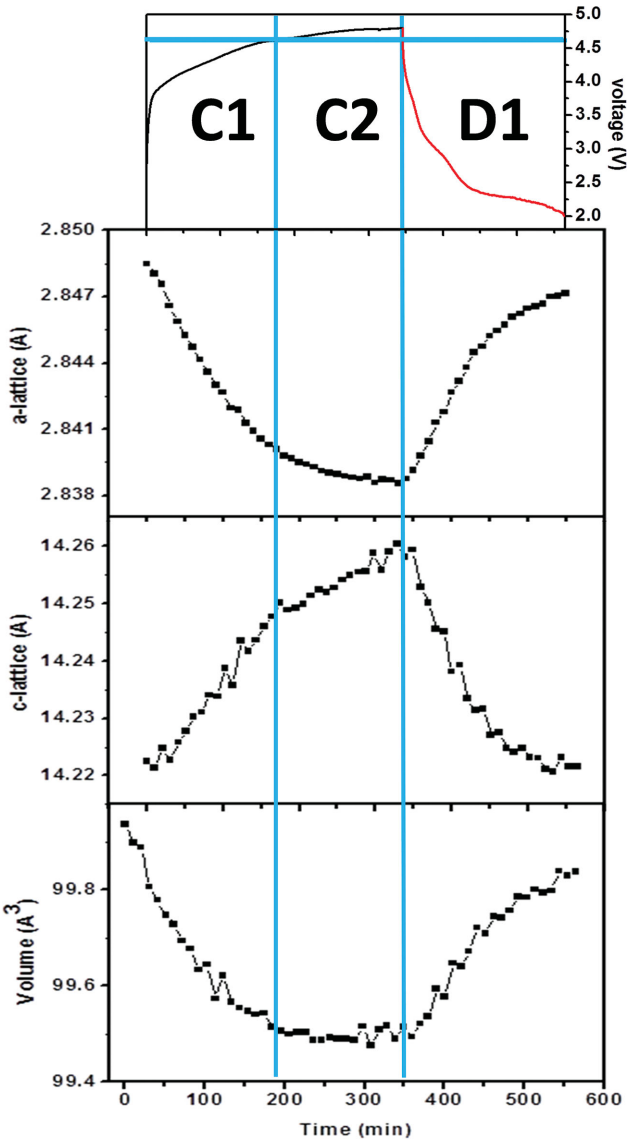

Figure 4. Change of the Rietveld refined *a* and *c*-lattice parameters and corresponding unit cell volume during the 1st cycle.

Figure 4: C1 for charging between open-circuit voltage to 4.6 V, C2 between 4.6 and 4.8 V and D1 for the whole discharge. For clearer observation, only the characteristic diffraction peaks of the cathode material: (003), $(020)_{mon}$, $(110)_{mon}$, (101), (104), (110), and (113) are presented. Figure 3a shows the stacked in situ XRD patterns. The red and black colors represent the corresponding charge and discharge processes. Figure 3b shows the color-coded time-resolved intensity plots in which a more straightforward detection on the evolution of the diffraction peaks in both intensity and position can be acquired by direct visual observation of the color distribution versus time. The reference color bar is located under each XRD peak/peak pair, respectively. In addition, the change of *a* and *c* lattice parameters of the monoclinic unit cell and the related cell volume calculated by Rietveld refinement were displayed versus time in Figure 4.

First, in the C1 region, the (003) peak shifts prominently to the lower 2θ range while the (104) and (113) peaks move toward the higher range, indicating a higher *d*-spacing of the Li layers in the unit cell. This is evidently supported by the steep increase of the *c*-parameter that can be explained by simple Li extraction from the Li layers that results in stronger electrostatic repulsion of the neighboring oxygen layers.[17,37] Conversely, the value of the *a*-parameter drops in C1 region. This is probably due to the oxidation of the Ni^{2+} (0.69 Å) to Ni^{3+} (0.56 Å) and further to Ni^{4+} (0.48 Å) that leads to smaller ionic radii and metal–metal interaction length.[37]

After C1, a long and flat charging plateau starts at around 4.6 V in region C2. The (003), (104) and (113) peaks follow the trend observed in region C1, although the change is slower. The *c*-parameter keeps increasing. It should be pointed out that the *c*-parameter in C2 region behaves totally differently from what reported previously where the *c*-parameter decreased significantly near 4.8 V due to the proposed Li extraction from the TM layers,[17,37] strongly implying the Li ions were extracted from the Li layers rather than the TM layers in our $Li_{1.87}Mn_{0.94}Ni_{0.19}O_3$ material in this high-voltage region. More importantly, from both the stacked linear diffraction pattern and the color-coded intensity plots in Figure 3, it can be found that the height and intensity of the $(020)_{mon}$ and $(110)_{mon}$ peaks are basically unchanged in both the C1 and C2 regions. In many reported Li-rich cathode materials, a large portion of the Li ions in the TM layers will be extracted during the high-voltage charging process in the 1st cycle, leading to the breakup of the $LiTM_6$ ordering and consequently, the decay or disappearance of the $(020)_{mon}$ and $(110)_{mon}$ diffraction peaks.[17,38] Therefore, the preservation of these peaks here provides strong evidence to the fact that the $LiTM_6$ ordering in the TM layers is stable and the Li ions are not extracted from the TM layer in the C2 voltage region. Moreover, the *c*-parameter increases more slowly in C2 than in C1, and this can be also explained by the release of oxygen in C2 region. For the *a*-parameter, the rapid decrease stops and it only slightly decreased within this region due to the further oxidation of tiny amount of residual Ni^{3+} and/or Mn^{3+}.[37,39] This means the average radii of the TM ions were almost stable in C2 region. As a result, it indicates that the well-known oxygen release reaction became the main source to compensate for the charge balance on Li extraction at the high charging voltage.[37]

In the D1 discharge region, an opposite shift of the (003) (104) and (113) peaks can be observed. The *c*-parameter decreases in the whole D1 region, indicating the reintercalation of Li ions into the Li layers that reduces electrostatic repulsion between oxygen layers and leads to contraction of the Li layers. In contrast, the *a*-parameter continually grows in this region mainly due to the reduction of Ni^{4+} and Mn^{4+} that increased the cation radii and metal–metal distance on average.[37]

To further investigate the crystal structure evolution of the $Li_{1.87}Mn_{0.94}Ni_{0.19}O_3$ composite during cycling, aberration-corrected high-angle annular-dark-field scanning transmission electron microscopy (HAADF-STEM) characterization was performed (**Figure 5**). Note that only heavy elements like Mn and Ni can be observed in HAADF-STEM images as white spots while light elements such as Li or O are invisible.[40] A highly crystallized layered structure with a layer distance of 0.47 nm of the pristine sample can be clearly detected from Figure 5a. Note that there are some while spots in the Li layers on the surface area with a thickness of around 2 nm, indicating a small amount of TM ions in the Li layers probably due to insufficient Li source during high temperature calcination. After the 1st cycle, the thickness of the surface layer with Li/TM mixing was

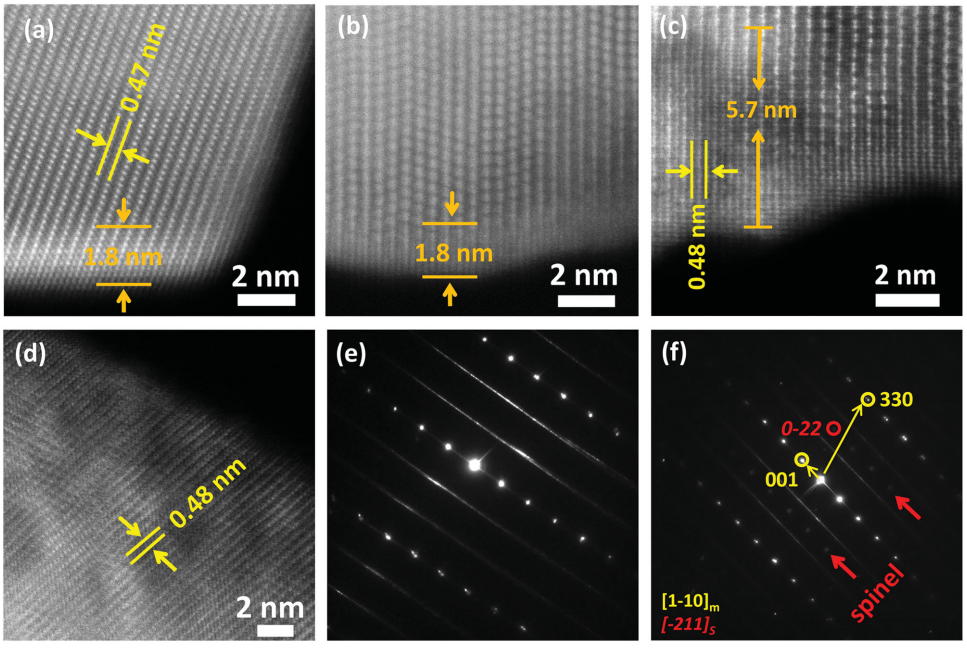

Figure 5. HAADF-STEM images of $Li_{1.87}Mn_{0.94}Ni_{0.19}O_3$ composite a) before cycling; b) after 1 cycle; c) after 10 cycles and d) after 50 cycles; and the corresponding SAED pattern of the sample along $[1\text{–}10]_{mon}$ e) after 1 cycle and f) 50 cycles, respectively.

almost the same as the pristine sample. This is consistent with the in situ XRD observation, further supporting that almost no TM ions diffused into the Li layers during the 1st cycle. After 10 electrochemical cycles, a significantly larger number of white spots can be found in the Li layers from the surface up to 7 nm into bulk area in Figure 5c, indicating prominent TM ions diffusion from the TM layers to the Li layers. After 50 cycles, some local reticulate patterns can be clearly observed on the original parallel lines over the whole crystal framework (Figure 5d). This has been demonstrated to be the characteristics of a defect spinel phase,[15,33,41] indicating large scale TM diffusion to the Li layers during the long-term cycling. Moreover, comparing the selected area electron diffusion (SAED) patterns of the sample after one cycle and 50 cycles (Figure 5e,f), extra spots (marked with red arrows) can be clearly identified between the diffuse scattering lines. These new spots can be well explained by a spinel phase which has evolved from the parent layered structure, further confirming the gradual TM ion diffusion and structure evolution during long-term electrochemical cycling.[41–43] More systematic HAADF-STEM observation associated with electron energy loss spectroscopy (EELS) can be very helpful to further investigate the structure evolution, oxygen coordination, and valence of TM ions during the Li_2MnO_3 activation process.[44,45] These advanced characterizations are on the way and the new results will be reported in a future study.

Based on the above results, the electrochemical behavior and corresponding structure evolution of our Ni-poor Li-rich cathode material during electrochemical cycling can be briefly illustrated in **Figure 6**. In the 1st charge, lattice oxygen ions close to the surface area where some TM ions that existed in the Li layers were extracted together with Li ions from the Li layers, while the Li and TM ions in the TM layers were relatively stable (Figure 6b). In fact, it was theoretically demonstrated in our earlier work that the energy barrier for oxygen removal is significantly lower (about 6 eV) if there is a neighboring Ni in the Li layer.[14] After that, less and less oxygen ions were further removed from the lattice and basically no more after the 5th charge. Meanwhile, as the capacity increased with more Li vacancies created in the Li layers, Li and TM ions in the TM layers gradually diffused into the Li layers (Figure 6d,e) as this is more energetically favorable with a lower Li concentration in the Li layer.[14,20] Additionally, when there is a neighboring oxygen vacancy, the TM, particularly the Ni in the TM layers will feature a much lower energy barrier to diffuse into the Li layers. As the TM ions continued to move into the Li layers and accumulated there, some localized spinel-like phase gradually formed with some Li ions occupying the tetrahedral sites in the Li layers (Figure 6f). It may be noted from the HAADF-STEM observation that the structure evolution appears to start from the surface and gradually extend to the bulk area. More importantly, in contrast to most Li-rich cathode materials,[15,16,38] basically no Li or TM extraction from the TM layers was detected in our $Li_{1.87}Mn_{0.94}Ni_{0.19}O_3$ material during the 1st high-voltage charge, which can be well attributed to the low Ni-doping. This strongly indicates that the oxygen release and TM rearrangement processes may not necessarily occur at the same time, and the latter plays a key role in determining the activation rate of the Li_2MnO_3 phase and consequently the specific capacity of Li-rich cathode materials. Moreover, the reaction kinetics of the TM rearrangement can be adjusted, for instance, by changing the ratio of Ni-doping.

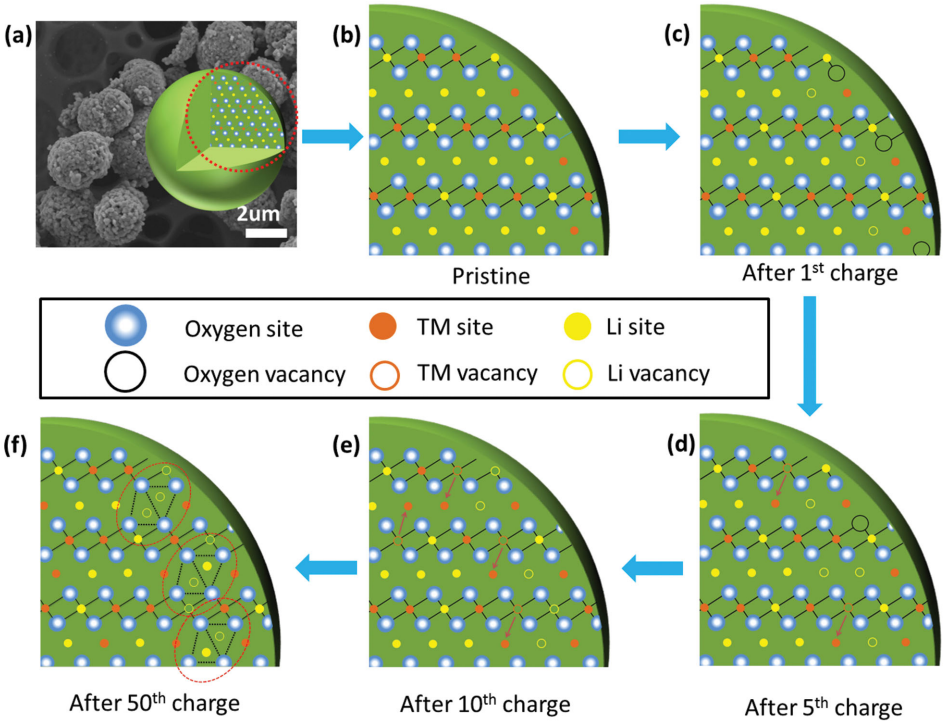

Figure 6. Schematic illustration of the crystal structure evolution of the $Li_{1.87}Mn_{0.94}Ni_{0.19}O_3$ material at different charged states.

3. Conclusions

Due to the low level of Ni-doping in our Li-rich cathode material $Li_{1.87}Mn_{0.94}Ni_{0.19}O_3$, the Li_2MnO_3 activation process was artificially retarded and split into dozens of cycles, providing excellent opportunity for us to probe the intermediate state, phase and subreactions of the Li-rich cathode materials. With detailed electrochemical measurements and material characterization including in situ XRD and HAADF-STEM observation, it was revealed that the Li extracted in the 1st charge was mainly from the Li layers, even at the high voltage range, with simultaneous oxygen generation. The $LiTM_6$ cation ordering in the TM layers was basically stable during the 1st charge. In addition, the oxygen generation stopped after the initial 5 cycles while the TM ions continued to diffuse from TM layers to the Li layers in all the following cycles, resulting in structure transformation from layered phase to a new spinel phase that is highly associated with the gradual capacity increase of the material. Based on these results, it can be deducted that the oxygen release reaction features a much faster kinetics than that of the phase transformation which involves the diffusion of both Li and TM ions from the TM layers to the Li layers, and the latter plays a key role in determining the capacity of the Li-rich cathode materials. This work not only provides insights in deeper understanding of the fundamental electrochemical reaction mechanisms and the original structure evolution of the Li-rich cathode materials, but also sheds light on the design and development of low-cost and high-energy cathode materials for next generation battery application.

4. Experimental Section

Materials Synthesis: All the chemicals were from Aldrich-Sigma without further purification. The $Li_{1.87}Mn_{0.94}Ni_{0.19}O_3$ cathode material synthesis was completed in two steps. First, stoichiometric $Mn(NO_3)_2$ and $Ni(NO_3)_2$ were dissolved in distilled water and then coprecipitated with an equal volume of 0.2 M sodium carbonate. The immediate light brown precipitate was aged at room temperature for 20 h, collected and then dried at 100 °C. After that, the precipitate was preheated at 500 °C in air for 5 h and then calcined with stoichiometric $LiOH{\cdot}H_2O$ at 900 °C in air for another 12 h to obtain the final product. An excess amount of 3 wt% $LiOH{\cdot}H_2O$ was used to compensate for loss of Li due to volatilization at this temperature.

Materials Characterization: The mole ratio of the metal elements was determined by a Varian 725-ES inductively coupled plasma atomic emission spectroscopy (ICP-AES). Ex situ powder XRD characterization for the pristine powder sample was conducted on a Bruker advanced x-ray diffractometer (40 kV, 30 mA) with Cu Kα (λ = 0.15406 nm) radiation at a scanning rate of 1° min^{-1}. High resolution synchrotron in situ X-ray diffraction patterns were collected in transmission mode on powder diffraction beamline of Australian Synchrotron using the MY THEN microstrip detector and a Si(111) monochromator with the wavelength of 0.8265 Å. 2θ zero-error were determined from a standard 0.3 mm capillary of a LaB_6/Si mixture using transmission geometry. Corresponding cycling test of the cell was conducted on a Neware electrochemical tester under a constant current density of 30 mAh g^{-1}.[46] Fundamental parameter (FP) approach was employed in TOPAS4.2 to perform whole-pattern profile fitting of the diffraction data. FE-SEM for all the samples was performed on JEOL 7800 equipment to investigate their morphological characteristics. STEM observation was conducted on JEM-ARM200F at 200kV with a HAADF detector. XPS analysis was carried out on a Kratos Axis Ultra X-ray photoelectron spectrometer with AlKα (1253.6 eV) X-ray. The measured binding energies were calibrated by the CasaXPS software with reference to the C 1s peak at 284.8 eV.

Electrochemical Test: All the electrochemical measurements were carried out in CR2032 coin cells at room temperature. First, a mixture of the active materials, acetylene black and polyvinylidene fluoride were mechanical ground in a mortar with a weight ratio of 7:2:1 and then coated as a slurry with appropriate amount of *N*-methyl-2-pyrrolidone onto aluminum foil using the doctor blade method. After that, the slurry was dried in a vacuum oven at 120 °C for 12 h and then cut into working electrodes with an area of 0.7 cm^2 and typical mass loading (active material) of about 2.12 mg cm^{-2}. The whole process of CR2032 coin cell fabrication was completed in an argon-filled glove box.

The as-prepared electrode was assembled as the cathode. Li foil and 1 M $LiPF_6$ in a mixture of ethylene carbonate (EC) and dimethyl carbonate (DMC) (1:1) were used as the negative electrode and electrolyte, respectively. The galvanostatic charge/discharge measurement was performed in a multichannel battery tester (Land CT2001A).

Acknowledgements

D.Y. acknowledges financial support from Chinese Scholarship Council (CSC) and authors are grateful to ARC through its LP and DP programs. The authors also thank Dr. Q. F. Gu of the Australian Synchrotron for their contributions on synchrotron XRD experiments and Dr. Guang Han for the technical support in SEM characterization.

Received: August 5, 2015
Revised: September 29, 2015
Published online: November 10, 2015

[1] O. K. Park, Y. Cho, S. Lee, H.-C. Yoo, H.-K. Song, J. Cho, *Energy Environ. Sci.* **2011**, *4*, 1621.
[2] B. Dunn, H. Kamath, J.-M. Tarascon, *Science* **2011**, *334*, 928.
[3] R. Van Noorden, *Nature* **2014**, *507*, 26.
[4] B. Luo , B. Wang, X. Li, Y. Jia, M. Liang, L. Zhi, *Adv. Mater.* **2012**, *24*, 3538.
[5] H. Wang, L.-F. Cui, Y. Yang, H. Sanchez Casalongue, J. T. Robinson, Y. Liang, Y. Cui, H. Dai, *J. Am. Chem. Soc.* **2010**, *132*, 13978.
[6] C. K. Chan, H. Peng, G. Liu, K. McIlwrath, X. F. Zhang, R. A. Huggins, Y. Cui, *Nat. Nanotechnol.* **2007**, *3*, 31.
[7] H. Yu, R. Ishikawa, Y. G. So, N. Shibata, T. Kudo, H. Zhou, Y. Ikuhara, *Angew. Chem. Int. Ed.* **2013**, *52*, 5969.
[8] M. M. Thackeray, S.-H. Kang, C. S. Johnson, J. T. Vaughey, R. Benedek, S. Hackney, *J. Mater. Chem.* **2007**, *17*, 3112.
[9] J. Zheng, M. Gu, J. Xiao, B. J. Polzin, P. Yan, X. Chen, C. Wang, J.-G. Zhang, *Chem. Mater.* **2014**, *26*, 6320.
[10] P. Oh, M. Ko, S. Myeong, Y. Kim, J. Cho, *Adv. Energy Mater.* **2014**, *4*, 1400631.
[11] H. Yu, H. Zhou, *J. Phys. Chem. Lett.* **2013**, *4*, 1268.
[12] S.-H. Park, S.-H. Kang, C. Johnson, K. Amine, M. Thackeray, *Electrochem. Commun.* **2007**, *9*, 262.
[13] M. Sathiya, A. M. Abakumov, D. Foix, G. Rousse, K. Ramesha, M. Saubanère, M. Doublet, H. Vezin, C. Laisa, A. Prakash, *Nat. Mater.* **2014**, *14*, 230.
[14] D. Ye, C. Sun, Y. Chen, K. Ozawa, D. Hulicova-Jurcakova, J. Zou, L. Wang, *Nano Res.* **2014**, *8*, 808.
[15] B. Xu, C. R. Fell, M. Chi, Y. S. Meng, *Energy Environ. Sci.* **2011**, *4*, 2223.
[16] A. R. Armstrong, M. Holzapfel, P. Novák, C. S. Johnson, S.-H. Kang, M. M. Thackeray, P. G. Bruce, *J. Am. Chem. Soc.* **2006**, *128*, 8694.

[17] Z. Lu, J. Dahn, *J. Electrochem. Soc.* **2002**, *149*, A815.
[18] A. D. Robertson, P. G. Bruce, *Chem. Mater.* **2003**, *15*, 1984.
[19] S. Hy, F. Felix, J. Rick, W.-N. Su, B. J. Hwang, *J. Am. Chem. Soc.* **2014**, *136*, 999.
[20] D. Ye, K. Ozawa, B. Wang, D. Hulicova-Jurcakova, J. Zou, C. Sun, L. Wang, *Nano Energy* **2014**, *6*, 92.
[21] D. Ye, B. Wang, Y. Chen, G. Han, Z. Zhang, D. Hulicova-Jurcakova, J. Zou, L. Wang, *J. Mater. Chem. A* **2014**, *2*, 18767.
[22] J. Bréger, M. Jiang, N. Dupré, Y. S. Meng, Y. Shao-Horn, G. Ceder, C. P. Grey, *J. Solid State Chem.* **2005**, *178*, 2575.
[23] K. A. Jarvis, M. Jiang, N. Dupré, Y. S. Meng, Y. Shao-Horn, G. Ceder, C. P. Grey, *Chem. Mater.* **2011**, *23*, 3614.
[24] Y. Li, Z. Zhou, M. Ren, X. Gao, J. Yan, *Electrochim. Acta* **2006**, *51*, 6498.
[25] E. Regan, T. Groutso, J. Metson, R. Steiner, B. Ammundsen, D. Hassell, P. Pickering, *Surf. Interface Anal.* **1999**, *27*, 1064.
[26] Z. Li, J. Wang, S. Liu, X. Liu, S. Yang, *J. Power Sources* **2011**, *196*, 8160.
[27] M. E. Spahr, P. Novák, B. Schnyder, O. Haas, R. Nesper, *J. Electrochem. Soc.* **1998**, *145*, 1113.
[28] N. Andreu, D. Flahaut, R. Dedryvère, M. Minvielle, H. Martinez, D. Gonbeau, *ACS Appl. Mater. Interfaces* **2015**, *7*, 6629.
[29] B. Song, M. O. Lai, Z. Liu, H. Liu, L. Lu, *J. Mater. Chem. A* **2013**, *1*, 9954.
[30] X. W. Lou, D. L. A. Archer, Z. Yang, *Adv. Mater.* **2008**, *20*, 3987.
[31] Y. Jiang, Z. Yang, W. Luo, X. Hu, Y. Huang, *Phys. Chem. Chem. Phys.* **2013**, *15*, 2954.
[32] A. W. Rowe, J. Dahn, *J. Electrochem. Soc.* **2014**, *161*, A308.
[33] M. Gu, I. Belharouak, J. Zheng, H. Wu, J. Xiao, A. Genc, K. Amine, S. Thevuthasan, D. R. Baer, J.-G. Zhang, *ACS Nano* **2012**, *7*, 760.
[34] B. Song, Z. Liu, M. O. Lai, L. Lu, *Phys. Chem. Chem. Phys.* **2012**, *14*, 12875.
[35] K. G. Gallagher, J. R. Croy, M. Balasubramanian, M. Bettge, D. P. Abraham, A. K. Burrell, M. M. Thackeray, *Electrochem. Commun.* **2013**, *33*, 96.
[36] F. Dogan, B. R. Long, J. R. Croy, K. G. Gallagher, H. Iddir, J. T. Russell, M. Balasubramanian, B. Key, *J. Am. Chem. Soc.* **2015**, *137*, 2328.
[37] D. Mohanty, S. Kalnaus, R. A. Meisner, K. J. Rhodes, J. Li, E. A. Payzant, D. L. Wood III, C. Daniel, *J. Power Sources* **2013**, *229*, 239.
[38] R. Wang, X. He, L. He, F. Wang, R. Xiao, L. Gu, H. Li, L. Chen, *Adv. Energy Mater.* **2013**, *3*, 1358.
[39] D. Mohanty, S. Kalnaus, R. A. Meisner, J. Li, E. A. Payzant, K. Rhodes, D. L. Wood III, C. Daniel, *RSC Adv.* **2013**, *3*, 7479.
[40] J. Bareno, C. Lei, J. Wen, S. H. Kang, I. Petrov, D. Abraham, *Adv. Mater.* **2010**, *22*, 1122.
[41] J. Zheng, P. Xu, M. Gu, J. Xiao, N. D. Browning, P. Yan, C. Wang, J.-G. Zhang, *Chem. Mater.* **2015**, *27*, 1381.
[42] A. Boulineau, L. Simonin, J.-F. o. Colin, E. Canévet, L. Daniel, S. b. Patoux, *Chem. Mater.* **2012**, *24*, 3558.
[43] A. Boulineau, L. Croguennec, C. Delmas, F. Weill, *Chem. Mater.* **2009**, *21*, 4216.
[44] J. Zheng, M. Gu, J. Xiao, P. Zuo, C. Wang, J.-G. Zhang, *Nano Lett.* **2013**, *13*, 3824.
[45] M. Gu, A. Genc, I. Belharouak, D. Wang, K. Amine, S. Thevuthasan, D. R. Baer, J.-G. Zhang, N. D. Browning, J. Liu, *Chem. Mater.* **2013**, *25*, 2319.
[46] W. R. Brant, S. Schmid, G. Du, Q. Gu, N. Sharma, *J. Power Sources* **2013**, *244*, 109.